Available online at www.sciencedirect.com
SCIENCE DIRECT®
Journal of Computational Physics 184 (2003) 339–365
JOURNAL OF COMPUTATIONAL PHYSICS
www.elsevier.com/locate/jcp

A time self-adaptive multilevel algorithm for large-eddy simulation

M. Terracol [a,*], P. Sagaut [a], C. Basdevant [b]

[a] *ONERA, 29 av. de la Division Leclerc, 92322 Châtillon Cedex, France*
[b] *Université Paris-Nord, LAGA UMR 7539, 99 Av J.B. Clément, 93430 Villetaneuse, France*

Received 15 January 2002; received in revised form 26 June 2002; accepted 27 September 2002

Abstract

An extension of the multilevel method applied to LES proposed in Terracol et al. [J. Comput. Phys. 167 (2001) 439] is introduced here to reduce the CPU times in unsteady simulation of turbulent flows. Flow variables are decomposed into several wavenumber bands, each band being associated to a computational grid in physical space. The general framework associated to such a decomposition is presented, and a new adapted closure is proposed for the subgrid terms which appear at each filtering level, while the closure at the finest level is performed with a classical LES model. CPU time saving is obtained by the use of *V*-cycles, as in the multigrid terminology. The main part of the simulation is thus performed on the coarse levels, while the smallest resolved scales are kept frozen (quasi-static approximation [Comput. Methods Appl. Mech. Engrg. 159 (1998) 123]). This allows to reduce significantly the CPU times in comparison with classical LES, while the accuracy of the simulation is preserved by the use of a fine discretization level. To ensure the validity of the quasi-static approximation, a dynamic evaluation of the time during which it remains valid is performed at each level through an a priori error estimation of the small-scales time variation. This leads to a totally self-adaptive method in which both the number of levels and the integration times on each grid level are evaluated dynamically. The method is assessed on a fully unsteady time-developing compressible mixing layer at a low-Reynolds number for which a DNS has also been performed, and in the inviscid case. Finally, a plane channel flow configuration has been considered. In all cases, the results obtained are in good agreement with classical LES performed on a fine grid, with CPU time reduction factors of up to five.

Keywords: Large-eddy simulation; Subgrid-scale modeling; Multilevel

1. Introduction

Large-eddy simulation (LES) is a widely used tool for the numerical simulation of unsteady turbulent flows. A reduction of the number of degrees of freedom of the simulation compared to direct numerical simulation (DNS) is obtained by resolving only the low-wavenumber modes of the flow, while the effect of

* Corresponding author.
E-mail address: terracol@onera.fr (M. Terracol).

0021-9991/02/$ - see front matter
PII: S0021-9991(02)00017-7

the unresolved high-wavenumber modes associated to unresolved small scales of motion (subgrid scales) are only taken into account through the use of a so-called subgrid model.

Despite the large amount of work dedicated to the development of new subgrid models, large-eddy simulation is still mostly limited to simple flows and low-Reynolds numbers when inhomogeneous flows are considered. This is due to the fact that the subgrid-viscosity models generally used in actual practical simulations have been developed in the framework of isotropic homogeneous turbulence, and are not able to take into account in a proper way physical phenomena such as inverse energy transfer from subgrid to resolved scales (backscatter), even with dynamic versions. Such eddy-viscosity models are so not able to account correctly for the presence of inhomogeneous subgrid scales, as in wall-bounded or separated flows. Some more complicated models such as mixed dynamic/scale-similarity models or deconvolution-like approaches can handle inhomogeneities of the flow, but generally remain more complex to use and/or more expensive than classical subgrid-viscosity models. These limitations lead to the use of fine computation grids to allow a quasi-deterministic representation of the smallest coherent structures of the flow. In return, a large number of meshpoints and very small time steps are involved, thus increasing the simulation cost. Despite the great increase of today's computers capabilities, only very few flows can be accurately simulated, generally in the limit of low-Reynolds numbers. Thus, a large amount of work should be dedicated to the reduction of the CPU costs of such simulations.

In previous works [30,34], the ability of a multilevel/multiresolution approach to provide reliable results has been investigated by multigrid-type computations in a plane channel flow configuration. Notice that the application of a multigrid methodology to large-eddy simulation had been proposed by Voke, with the "multimesh" concept [35], but was limited to quasi-steady applications because of an unfortunate choice of too long integration times on each grid. The approach described in [30,34] relies on a quasi-static approximation of the smallest resolved scales, which are kept frozen during time integration on the coarse levels. The general idea of these works was inspired from the works of Dubois et al. [10] and Debussche et al. [5], where a derivation and analysis of a multilevel approach in spectral space, the non-linear Galerkin method, and of the quasi-static approximation have been provided in the case of incompressible flows. In the multilevel approach presented in [30,34], the use of different grid levels involves naturally a scale-separation of the flow variables, leading to a multilevel decomposition. The general mathematical multiresolution framework linked to this feature has been presented in [30], and can be related to the multiresolution formalism introduced by Harten [13]. In that paper, the scale-separation associated to the Reynolds averaged Navier–Stokes methodologies had also been considered. From these works, it results that the multilevel scale-separation involves different subgrid terms at each level of resolution that require a mathematical closure. In [34], an adapted subgrid model based on the use of a multilevel self-similarity term combined with an eddy-viscosity term computed following the dynamic procedure from Germano [11] has been proposed and assessed in a compressible plane channel flow configuration.

Here, a rather similar methodology is proposed as follows: as in [30,34], a hierarchy of several filtering levels, defined implicitly by nested overlapping grids is introduced. Then, CPU-time saving is obtained by the use of a V-cycling strategy between the grids, similar to the one used in steady multigrid algorithms. The main part of the simulation is thus performed on the coarsest grids, with less points and and larger time steps than the finest ones. Indeed, the time step at each grid level is classically chosen to satisfy the CFL stability condition, which leads to larger time steps on the coarse grids, since a constant value of the CFL number is adopted between the different grid levels. The application of such a strategy to unsteady flows is founded on the quasi-static approximation of the small scales introduced by Dubois et al. [10], which allows to freeze the smallest resolved scales of a filtering level during a "short" integration time on the coarser levels.

While in [34] the number of time steps performed at each level during one V-cycle was fixed arbitrarily, the present study proposes a self-adaptive cycling strategy in time based on a priori error

estimates. In this strategy, the integration times of all grid levels are computed dynamically by the use of a small-scales error parameter which controls the validity of the quasi-static approximation at each filtering level.

Moreover, it was shown in [34] that an adapted multilevel subgrid closure is required at each level of resolution. Such a closure has to take into account explicitly the information resolved on the finer levels. In [34], a closure based on the dynamic mixed methodology of Zang et al. [38] has been proposed and assessed. In the present study, a new, simpler closure is introduced. It is simply based on a generalization of Germano's identity which allows to express the subgrid terms at each level of resolution as a function of the subgrid terms at finer levels. Moreover, this closure is very general, and does not require classical commutation hypothesis between filtering and space derivatives.

In Section 2, the general multilevel framework linked to the algorithm is presented. A parallel can be drawn with the multiresolution framework introduced by Harten [13]. The new multilevel closure is then presented. Section 3 deals with the self-adaptive methodology, where the V-cycling strategy and the dynamic integration times estimation process are detailed.

The algorithm is then first assessed in Section 4 by numerical simulations of a time-developing mixing layer. First, a low-Reynolds number is considered, and the results are compared to those from a well-resolved eight-eddy direct numerical simulation. The robustness of the method is then controlled by numerical tests in an inviscid mixing layer. Finally, the method is applied in Section 5 to the simulation of a plane channel flow to assess it in the case of inhomogeneous flows with "complex" boundary conditions such as walls. In this last case, a rather high value of the Reynolds number has been considered.

2. Multilevel framework

2.1. Multilevel decomposition

We introduce the framework of a multilevel decomposition of any variable ϕ of the flow by the use of N different filtering levels. Each level is defined by mean of a family of low-pass filters $\{G_n\},\ n \in [1,N]$ which are characterized by their cutoff lengthscales Δ_n, associated to the cutoff wave numbers k_n in spectral space. Any filtered variable is then formally defined as the convolution product of the continuous variable with the filter kernel G_n

$$G_n * \phi(x,t) = \int_\Omega G_n(\Delta_n(x,t), x-\xi)\phi(\xi,t)\,\mathrm{d}\xi, \tag{1}$$

where $x \in \Omega \subset \mathbb{R}^3$ is the space coordinates vector and $t \in \mathbb{R}^+$ is time. In the following, all the developments will be classically made in the simple case of a spatial and isotropic filtering of the solution, e.g., $\Delta_n(x,t) = \Delta_n$. Some more general extensions can however be found in literature, such as the works of Dakhoul and Bedford [3,4], or more recently those of Pruett [26] or Carati and Wray [1], who propose to explicitly take into account the temporal filtering.

Hereafter, the case $\Delta_{n+1} \geqslant 2\Delta_n$ will be considered, or equivalently $k_{n+1} \leqslant k_n/2$. The filtered variables at the finest level of resolution are defined as $\overline{\phi}^{(1)} = G_1 * \phi$. The filtered variables at any level $n \in [2,N]$ are then recursively defined as

$$\overline{\phi}^{(n)} = G_n * G_{n-1} * \cdots * G_2 * G_1 * \phi = \mathscr{G}_1^n(\phi), \tag{2}$$

with, for any $m \in [1,n]$: $\mathscr{G}_m^n(\cdot) = G_n * G_{n-1} * \cdots G_{m+1} * G_m * (\cdot)$.

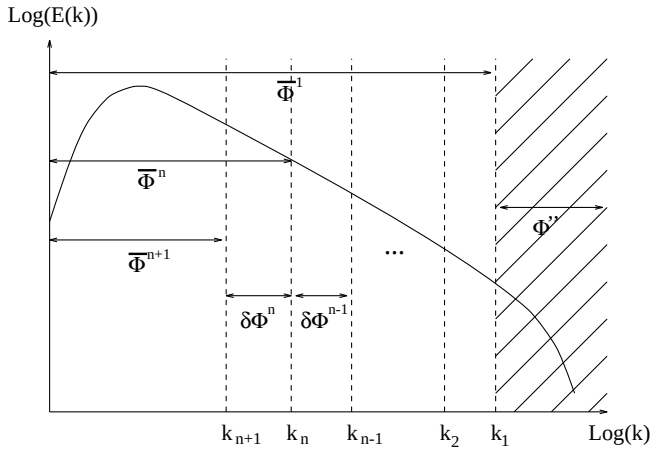

Fig. 1. Multilevel decomposition.

Each flow variable ϕ can then be decomposed as

$$\phi = \overline{\phi}^{(n)} + \sum_{l=1}^{n-1} \delta\phi^l + \phi'', \tag{3}$$

where $\delta\phi^l = \overline{\phi}^{(l)} - \overline{\phi}^{(l+1)}$ and $\phi'' = \phi - \overline{\phi}^{(1)} = \delta\phi^0$.

In the compressible case, Favre density-weighted filtering is prescribed, and will be used in the following, i.e., each density-weighted-filtered variable will be defined as

$$\widetilde{\phi}^{(n)} = \frac{\overline{\rho\phi}^{(n)}}{\overline{\rho}^{(n)}}, \tag{4}$$

where ρ denotes density. In the multilevel decomposition (3), $\overline{\phi}^{(n)}$ corresponds to the resolved scales at the nth level of resolution. The details $\delta\phi^l$ correspond to the scales resolved at the level l, which are unresolved at the level $l+1$, and ϕ'' corresponds to the finest level unresolved scales. Fig. 1 illustrates schematically this decomposition of the flow in spectral space, for the case of a family of sharp-cut-off filters.

Notice that for $N = 1$, the decomposition (3) simplifies into the classical LES decomposition between resolved and subgrid scales.

2.2. Basic equations

We consider the dimensionless compressible Navier–Stokes equations, written under the following compact form:

$$\frac{\partial V}{\partial t} + \mathcal{N}(V) = 0, \tag{5}$$

where $V = (\rho, \rho U^{\mathrm{T}}, \rho E)^{\mathrm{T}}$, $U = (u_1, u_2, u_3)^{\mathrm{T}}$ and

$$\mathcal{N}(V) = \begin{pmatrix} \nabla\cdot(\rho U) \\ \nabla\cdot(\rho U\otimes U) + \nabla p - \nabla\cdot\sigma \\ \nabla\cdot((\rho E + p)U) - \nabla\cdot(\sigma : U) + \nabla\cdot Q \end{pmatrix},$$

where p is the pressure, ρ the density, U the velocity vector, ρE the total energy, σ the viscous stress tensor, and Q the viscous heat flux vector (see [34] for detailed expressions).

In the following, simple notations will be used: the vector associated to the resolved flow variables at level n will be noted simply $\overline{V}^{(n)}$. However, since we consider here the compressible case, Favre filtering of the variables is performed. That is to say that the variables on which the filtering operation is applied are ρ, ρU, and p or equivalently ρT. That implies that the fifth component of the filtered field $\overline{V}^{(n)}$ is not the filtered energy, but the resolved energy at level n, linked to the resolved density, velocity and pressure fields at level n

$$\overline{V}_5^{(n)} = \widehat{\rho E}^{(n)} = \frac{\overline{p}^{(n)}}{(\gamma-1)} + \frac{1}{2}\frac{\overline{\rho U}^{(n)} \cdot \overline{\rho U}^{(n)}}{\overline{\rho}^{(n)}} \neq \overline{\rho E}^{(n)}.$$

For any $n \in [1, N]$, the application of the operator $\mathscr{G}_1^n$ to Eq. (5) and the assumption that the filters G_l, $l \in [1, N]$ commute with time derivatives, lead to the filtered equations at the level n

$$\frac{\partial \overline{V}^{(n)}}{\partial t} + \mathscr{N}(\overline{V}^{(n)}) = -\mathscr{T}^{(n)}, \tag{6}$$

where $\mathscr{T}^{(n)}$ is the subgrid term defined as

$$\mathscr{T}^{(n)} = \overline{\mathscr{N}(V)}^{(n)} - \mathscr{N}(\overline{V}^{(n)}). \tag{7}$$

It should be remarked that commutation errors between space derivatives and filters are included in the general expression considered for $\mathscr{T}^{(n)}$. However, if the filters used are commutative with space derivatives, the only remaining term in $\mathscr{T}^{(n)}$ comes from the non-linear (convective) term.

2.3. Multilevel subgrid closure

At each resolution level n, the subgrid term $\mathscr{T}^{(n)}$ requires a closure because the quantity $\overline{\mathscr{N}(V)}^{(n)}$ remains unknown. By recurrence, the following relation is obtained

$$\mathscr{T}^{(n)} = \sum_{l=1}^{n-1} \mathscr{G}_{l+2}^n (G_{l+1} * \mathscr{N}(\overline{V}^{(l)}) - \mathscr{N}(\overline{V}^{(l+1)})) + \mathscr{G}_2^n(\mathscr{T}^{(1)}). \tag{8}$$

In this relation, the only term that needs to be parametrized is $\mathscr{T}^{(1)}$, corresponding to interactions with the unresolved scales from the finest level. Provided that k_1 is sufficiently large, a simple LES closure (see [28] for a review) – and even no closure if k_1 is close to Kolmogorov wave number – can be used at the first level for an accurate evaluation of $\mathscr{T}^{(1)}$. On the coarser levels, the subgrid terms can then be simply evaluated by relation (8). Notice that in this general relation, no assumption about commutativity of the filtering operation with space derivatives is used. This last point can be of great interest for applications using non-uniform meshes where commutation errors may occur. Moreover, all the non-linearities of the subgrid terms can be taken into account, while classical closures neglect the subgrid terms associated to the non-linear expressions of the viscous terms σ and Q. Finally, since the first term in the RHS of (8) corresponding to local interactions between wavenumbers should be dominant (see [6,17,18] for instance), both the dissipative forward transfer and the anti-dissipative backscatter of energy are represented, while traditional eddy-viscosity models are strictly dissipative.

A rather similar relation can be found in the paper of Maurer and Fey [22], but with the requirement of a particular commutation hypothesis between the filter and the Navier–Stokes operator. In that work, this relation was used to get a scale-similarity model for the subgrid terms at the fine level.

It should be noted that relation (8) can be interpreted as a N-level generalization of the well-known Germano's identity [11]. In particular, it can simply be re-written as

$$\mathscr{T}^{(n+1)} - G_{n+1} * \mathscr{T}^{(n)} = G_{n+1} * \mathscr{N}(\overline{V}^{(n)}) - \mathscr{N}(\overline{V}^{(n+1)}), \tag{9}$$

which falls into the original Germano's identity when $n = 1$ and when commutativity of the filters with space derivatives is assumed.

Deconvolution methods can eventually be considered as a particular multilevel formalism. Indeed, these methods involve two different filtering levels. The computation is performed at level 2, while a subgrid closure at this level is obtained by getting an approximation of the field at level 1 by approximate inverse filtering. The subgrid terms are then computed as $\mathscr{T}^{(2)} = G_2 * \mathscr{N}(\overline{V}^{(1)}) - \mathscr{N}(\overline{V}^{(2)})$, which is a particular case of relation (8) in which n is set to 2, and the second term in the right-hand side is neglected. That is to say that it is assumed that interactions with wave numbers greater than k_1 are neglected, following the conclusions of Kraichnan [18], Kerr et al. [17], and Domaradzki et al. [6]. Nevertheless, a correction term is generally added to the filtered equations to drain more energy from the resolved scales. In particular, Stolz et al. [32] add a regularization term in the filtered equations by mean of a secondary filter. Domaradzki and Yee [9], in the extension of the velocity estimation model to high Reynolds numbers, after a deconvolution step, perform an integration of the whole field at a finer grid level to account for distant interactions.

3. Time self-adaptive procedure

3.1. Discrete multilevel formalism

From a practical point of view, the finest filtering level is implicitly defined by the space discretization, as it is generally the case in large-eddy simulation. That is to say that the effective cut-off wave number of level 1 coincide with the numerical one (i.e., the Nyquist wave number defined as $k_{\text{num}} = \pi/\Delta_1$, where Δ_1 represents the finest level mesh spacing).

Several methods make it possible to get a multilevel scale-separation from the finest resolved field in physical space. All of them rely on the use of discrete filtering operators which can be Padé approximants of known continuous filters (Gaussian filter for instance), as in [32,33], or simple approximations based on Taylor series expansions [29,31]. In the present paper, the scale-separation is obtained through the use of a hierarchy of embedded grids, as it was already the case in [30,34]. For any field $\overline{\phi}^{(n)}$ on the nth grid level, the field $\overline{\phi}^{(n+1)}$ on the coarser grid level corresponding to the $(n+1)$th filtering level is given by $\overline{\phi}^{(n+1)} = R_n^{n+1}(\overline{\phi}^{(n)})$, where R_n^{n+1} is a fine-to-coarse restriction operator acting as a discrete filter on the solution. The frequency complement $\delta\phi^n$ between the two levels n and $n+1$ is simply given on the nth grid level by: $\delta\phi^n = \overline{\phi}^{(n)} - P_{n+1}^n(\overline{\phi}^{(n+1)})$ $= (Id^n - P_{n+1o}^n R_n^{n+1})(\overline{\phi}^{(n)})$, where P_{n+1}^n is a coarse-to-fine prolongation operator that should be chosen as close as possible from the identity operator of level $(n+1)$.

This hierarchy of N embedded grids realises a N-level multilevel decomposition of the flow as described in the previous section, in which each continuous filtering operator G_n is formally equivalent to the discrete one R_{n-1}^n, and each level cut-off wavenumber k_n is implicitly defined by the filtering operation R_{n-1}^n and by the numerical cut-off wave number of the grid n.

Remark. It should be noticed that in the particular case considered here of a multigrid scale decomposition, the proposed hierarchical multilevel closure reads from (9):

$$\mathscr{T}^{(n)} = R_{n-1}^n(\mathscr{T}^{(n-1)}) + R_{n-1}^n(\mathscr{N}(\overline{V}^{(n-1)})) - \mathscr{N}(\overline{V}^{(n)}). \tag{10}$$

This last expression is identical to the classical deficit correction used in classical steady multigrid-type computations. Such a remark emphasizes the strong link between multigrid and multiscale methodologies. Indeed, in our case, the mathematical closure used in multigrid appears equivalent to a subgrid closure at each level of resolution.

3.2. Time-adaptive multigrid cycling procedure

In the present paper, a simple V-cycling strategy in time has been retained. It is an extension of the one used in steady multigrid algorithms. Such an algorithm was also proposed by Harten [13] in the multiresolution context. For a given number of levels N, one cycle is defined as follows:

1. $n = 1$.
2. Application of the numerical scheme to $\overline{\phi}^{(n)}$ during the integration time Δt_n.
3. *Restriction step:* if $n < N$, computation of the resolved field at level $n+1$ by application of the restriction operator: $\overline{\phi}^{(n+1)} = R_n^{n+1}(\overline{\phi}^{(n)})$, and computation of the frequency complement between the two levels n and $n+1$, kept stored at level n: $\delta\phi^{(n)} = \overline{\phi}^{(n)} - P_{n+1}^{n} \circ R_n^{n+1}(\overline{\phi}^{(n)})$.
4. If $n < N$, $n \leftarrow n+1$ and goto step 2.
5. *Prolongation step:* $\overline{\phi}^{(n-1)} = P_n^{n-1}(\overline{\phi}^{(n)}) + \delta\phi^{(n-1)}$.
6. If $n > 2$, $n \leftarrow n-1$ and goto step 5.
7. Goto step 1.

Remark. At each prolongation step, the frozen frequency complement is added to the low-wavenumber field. That is to say that the value of $\overline{\phi}^{(n)}$ at the time $t + \sum_{l=n+1}^{N} \Delta t_l$ is computed as:

$$\overline{\phi}^{(n)}\left(t + \sum_{l=n+1}^{N} \Delta t_l\right) = P_{n+1}^{n}(\overline{\phi}^{(n+1)}\left(t + \sum_{l=n+1}^{N} \Delta t_l\right)) + \delta\phi^{(n)}(t). \tag{11}$$

This cycling strategy can be used for unsteady simulations provided the quasi-static approximation [10] is satisfied at each filtering level. That is to say that the time variation of the frequency complement $\delta\phi^n$ of any variable ϕ can be neglected during the time integration on the coarser grid levels $l > n$. It relies on the works of Dubois et al. [10] who concluded that the smallest scales of the flow require less accuracy in time than the large energy-containing ones, and in particular can be frozen during short time intervals. This can be explained by the fact that large and small scales have a very different behavior, and that small scales reach equilibrium more quickly. In particular, Debussche et al. [5] have proved theoretically that the frozen-flow hypothesis related to the quasi-static approximation is appropriate for scales in the inertial range. For more general cases however, the resolution process based on the quasi-static approximation may not be interpreted as a rigorous resolution of all the scales. Indeed, some modeling terms arise at each interface between each filter scale, with consequently some modeling errors. However, on the coarse resolution levels ($n \geqslant 2$), the subgrid closure used is based on finer scales than the resolved ones, as it is the case in deconvolution approaches (see [32,33] for instance) or in the velocity estimation model of Domaradzki and co-workers [7–9], or in the variational multiscale method of Hugues et al. [15,16]. This closure is thus expected to be much more accurate than classical ones. The proposed algorithm may thus be interpreted as an accurate resolution of the largest energy-containing scales of the flow, while the small scales are regenerated and recorrelated to the large-scale flow locally in time, by non-linear interactions between the well-resolved large scales of interest.

One originality of the present approach is to proceed dynamically at each level n to an estimation of the time during which the quasi-static approximation of the small scales remains valid and time integration on coarser grids is allowed, and also to the evaluation of the number of levels to be considered. This algorithm

follows the same general ideas as the one proposed by Debussche et al. [5] in the non-linear Galerkin method. This is achieved by the use of a parameter $\varepsilon_{\max}$ which represents at each level n the maximum value allowed for the relative variation of the total energy associated to the small scales in the range $k_{n+1} < k < k_n$. The self-adaptive procedure, which is based on an a priori error estimate, consists of three main steps (Fig. 2 summarizes one time-integration cycle with all the notations introduced here):

1. First, the time τ_{QS} during which the quasi-static approximation will remain valid at the finest filtering level is estimated such that

$$\tau_{QS}\left\|\frac{\partial}{\partial t}\delta e^{(1)}\right\|_2 \Big/ \left\|\widehat{\rho E}^{(1)}\right\|_2 \leqslant \varepsilon_{\max}, \tag{12}$$

where

$$\widehat{\rho E}^{(n)} = \frac{\overline{p}^{(n)}}{(\gamma-1)} + \frac{1}{2}\frac{\overline{\rho U}^{(n)}.\overline{\rho U}^{(n)}}{\overline{\rho}^{(n)}}, \quad \delta e^{(n)} = \widehat{\rho E}^{(n)} - P^n_{n+1}(\widehat{\rho E}^{(n+1)}) \quad \text{and} \quad \|.\|_2 \text{ is the } \mathscr{L}_2\text{-norm.}$$

The time derivative in (12) is simply evaluated by a backward first-order approximation.

Relation (12) then provides an estimate of the maximum time during which the quasi-static approximation will remain valid at the finest filtering level:

$$\tau_{QS} = \varepsilon_{\max}\left\|\widehat{\rho E}^{(1)}\right\|_2 \Big/ \left\|\frac{\partial}{\partial t}\delta e^{(1)}\right\|_2. \tag{13}$$

The maximum number of levels N that can be considered is then estimated such that a minimum of one time-step satisfying the CFL condition can be performed at each coarse grid level. By denoting $\Delta t^{(n)}$ the time step of level n satisfying the CFL stability condition for the physical scales resolved at level n, the following relation is obtained:

$$\sum_{l=2}^{N} \Delta t^{(l)} \leqslant \tau_{QS}. \tag{14}$$

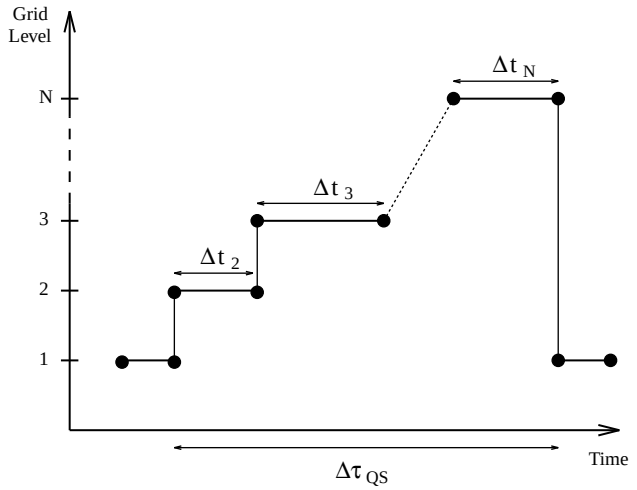

Fig. 2. Sketch of one dynamic time-integration cycle. $\Delta t_n = N_{it}^{(n)}\Delta t^{(n)}$; $\Delta\tau_{QS} = \sum_{l=2}^{N}\Delta t_l$.

A constant aspect ratio r in each direction is then considered for two successive grid levels. We thus have for any level $n \geqslant 2$: $\Delta t^{(n)} = r^{n-2}\Delta t^{(2)}$. Relation (14) can then be rewritten as

$$\sum_{l=2}^{N} r^{l-1} \leqslant \frac{\tau_{\mathrm{QS}}}{\Delta t^{(2)}}, \tag{15}$$

which finally gives

$$r^{N-1} - 1 \leqslant \frac{\tau_{\mathrm{QS}}}{\Delta t^{(2)}}. \tag{16}$$

The maximum number of levels that can be considered is finally given from (16) by

$$N = 1 + \mathscr{E}\left(\frac{\log(\tau_{\mathrm{QS}}/\Delta t^{(2)} + 1)}{\log(r)}\right), \tag{17}$$

where $\mathscr{E}$ stands for the integer part. In practice, the maximum number of levels to be considered can also be bounded to avoid the use of too coarse levels on which the number of meshpoints becomes too low to perform a numerical simulation.

2. The second step consists in the determination of the different levels integration times. At each level n, this time is referred to as Δt_n. These times are evaluated to ensure the validity of the quasi-static approximation of the small scales of any level during the time integration process on coarser levels, e.g., that the relative time variation of the smallest resolved scales from level $n-1$ will remain small during time integration on levels $l \geqslant n$. This condition is ensured by the following relation:

$$\left(\sum_{l=n}^{N} \Delta t_l\right) \left\| \frac{\partial}{\partial t} \delta e^{(n-1)} \right\|_2 \Big/ \left\| \widehat{\rho E}^{(n-1)} \right\|_2 \leqslant \varepsilon_{\max}. \tag{18}$$

This relation leads to the following upper triangular system:

$$\left(\sum_{l=n}^{N} \Delta t_l\right) = \varepsilon_{\max} \left\| \widehat{\rho E}^{(n-1)} \right\|_2 \Big/ \left\| \frac{\partial}{\partial t} \delta e^{(n-1)} \right\|_2 \quad \text{for } 2 \leqslant n \leqslant N. \tag{19}$$

This system can be solved trivially. However, one must ensure that $\Delta t_n > 0$ for any n. System (19) is solved recursively from $n = N$ to 2. If, at any given level l, $\Delta t_l < 0$, then the value of the integration time at level N is decreased of one time step $\Delta t_N \leftarrow \Delta t_N - \Delta t^{(N)}$. If the given value is negative, the number of levels is also decreased by one: $N \leftarrow N - 1$. In any case, the recursive system resolution process is then started again from level $N-1$ to level 2. The set of integration times obtained by this process does not satisfy the equality (19) in any case, but the inequality (18) is always verified, while all the integration times remain positive.

3. Finally, the number of time steps $N_{\mathrm{it}}^{(n)}$ allowed at each level $2 \leqslant n \leqslant N$ is simply computed as:

$$N_{\mathrm{it}}^{(n)} = \mathscr{E}\left(\frac{\Delta t_n}{\Delta t^{(n)}}\right). \tag{20}$$

If the value of $N_{\mathrm{it}}^{(n)}$ given by this relation is equal to zero, it is reset to one, and the CFL number at level n is then multiplied by the factor $\Delta t_n/\Delta t^{(n)}$. At each cycle, only one time step satisfying the CFL condition is performed at the finest level $n = 1$ to minimize the CPU costs. This of course does not ensure that the smallest resolved scales can evolve enough to remain in statistical equilibrium with the largest ones during this time. However, if the integration time at the finest resolution level is not sufficient to recorrelate the small scales with the large ones, the quasi-static approximation will not be satisfied for the next cycle which will thus be automatically shortened on the coarse levels by the self-adaptive algorithm.

In this strategy, the choice of the parameter $\varepsilon_{\max}$ remains empirical, but quite important, since it is linked to the error commited on the smallest scales of the flow. In practice, this parameter must be chosen to avoid a too important time decorrelation between large and small scales, which can lead to poor results and/or numerical instabilities.

3.3. Numerical scheme

The numerical method that has been retained in this study is the same that was already used in [34]: a classical cell-centered finite-volume scheme is used for space discretization, in which the convective fluxes are evaluated under their skew-symmetric form [19,37] to reduce aliasing errors, and the viscous ones using a staggered formulation. The time integration is performed using a classical third-order low-storage Runge–Kutta scheme [37].

This leads to a non-dissipative scheme which is second-order accurate in space, and third-order accurate in time. The grid transfer operators used in all the multilevel simulations are the third-order accurate non-dissipative operators detailed in [34].

4. Application 1: compressible mixing layer

First, the proposed algorithm has been applied to the case of a time-developing compressible mixing layer [2,24,36]. This flow is a typical example of a fully unsteady case, in which different scales, both in space and time are present.

First, the case of a low-Reynolds number has been considered, to show that the use of the time-adaptive cycling strategy coupled with the multilevel closure allows to recover results in good agreement with those from a fine monolevel LES when the effects of the subgrid model on both the two levels of resolution remain low. The results are also compared to those from a well-resolved DNS.

Then, the robustness and real performances of the multilevel subgrid closure are evaluated in the limit of an infinite Reynolds number; in this inviscid case, the only dissipation present in the simulation at each level of resolution is due to the subgrid model used.

In all the multilevel simulations performed in this section, the maximum number of levels allowed in the algorithm has been bounded to two. Indeed, the grids used for LES are relatively coarse and would not lead to a reasonable third grid level in terms of number of points in each space direction. Three-level computations will however be performed in the channel flow section in which bigger computational grids have been considered.

4.1. Low-Reynolds case

This case has been extensively studied in the LES context in the reference paper of Vreman et al. [36], where a critical comparison of several subgrid models has been performed by comparing LES results with those from a well-resolved DNS. The configuration retained in that paper was a four-roller simulation, thus allowing only two successive pairings of the primary vortices to occur. However, the experimental results of Huang and Ho [14] show that a fully turbulent state is only reached after the second pairing, with a small-scale transition and the establishment of a $k^{-5/3}$ spectrum. Thus, an eight-eddy simulation seems to be the minimal requirement to get an evaluation of the real potentialities of a subgrid model (P. Comte, private communication). Indeed, the flow is still strongly affected by the initial conditions before the second pairing, while it saturates and becomes unphysical afterwards if no other pairing is allowed in the computational domain. Thus a direct numerical simulation of an eight-eddy configuration has been performed, and then been used as a reference for large-eddy and multilevel simulations.

4.1.1. Direct numerical simulation

The computational domain considered here is a rectangular box $[0;L_x]\times[-L_y/2;L_y/2]\times[0;L_z]$, of dimensions $L_x=L_y=2$, and $L_z=1$. This domain is twice longer and higher than in [36]. Periodic boundary conditions are imposed in the streamwise (x) and spanwise (z) directions, while an outflow condition is used for the boundaries in the normal (y) direction. The direct numerical simulation has been performed on a $256\times192\times192$ computational grid, which is uniform in the streamwise and spanwise directions. In the normal direction, the mesh is uniform in the zone $[-L_y/8;L_y/8]$, where half the number of meshpoints are located, while grid stretching using an hyperbolic tangent law progression is used in the two zones $|y|>L_y/8$.

The simulation is initiated by an hyperbolic-tangent-law profile for the streamwise velocity component:

$$u_1(y,t=0)=U_\infty\tanh\left(\frac{2y}{\delta_0}\right), \tag{21}$$

where $U_\infty=1$ and $\delta_0=1/7N_{\mathrm{rol}}$ is the initial vorticity thickness. The value of L_x and L_y retained in this study are large enough to set the number of primary rollers of the simulation to $N_{\mathrm{rol}}=8$, and thus allow three successive pairings of these structures to occur. Other components of the mean velocity field are set to zero.

The initial mean density is uniform ($\rho=1$), and the mean temperature is given by the Busemann–Crocco law [27]

$$T=1+\tfrac{1}{2}(\gamma-1)M^2(1-u_1)^2. \tag{22}$$

The Mach number of the simulation is $M=0.2$, and the Reynolds number based on the upper velocity U_∞, and on the initial vorticity thickness δ_0 is $Re_{\delta_0}=100$, which is small enough to allow DNS, but also large enough to allow mixing transition.

As in [36], two- and three-dimensional modes are superimposed on the mean profiles. Each mode is noted (α,β), where α is the streamwise and β is the spanwise wavenumber. The two dimensional modes are $(8,0)$, $(4,0)$, $(2,0)$, and $(1,0)$, where $(8,0)$ is the most unstable mode given by linear stability analysis, with wavelength $L_x/8$, and the subharmonic modes $(4,0)$, $(2,0)$, and $(1,0)$ allow to initiate vortex pairings. The oblique modes $(8,8)$, $(8,-8)$, $(4,4)$, $(4,-4)$, $(2,2)$, $(2,-2)$, $(1,1)$, and $(1,-1)$ are also added to the initial field to introduce three-dimensionality. The symmetry of the initial conditions is removed by random phase shifts in the oblique modes. Unlike Vreman et al., the amplitude of the disturbances is the same for the two- and three-dimensional perturbations, and is set to 5×10^{-2}. Finally, all the perturbations are modulated in space by a Gaussian profile $f(y)=\exp(-0.5(y/(\delta_0)^2))$ to limit their effect to the initial rotational zone.

The simulation is conducted from $t=0$ to 140, where t is the time scaled by δ_0/U_∞. Primary rollers form at $t\simeq10$, and three successive pairings occur respectively at $t\simeq30,\ 50$, and 100. It is to be noted that due to the three-dimensional perturbation added on the initial mean profiles, the flow becomes quickly and strongly three-dimensional, with helicoidal pairings, as sketched in [2]. A mixing transition occurs between the first and second pairings, and the flow then reaches a fully turbulent state. Since the Reynolds number is rather low, viscous effects are very important. Indeed, energy spectra reveal only a short inertial range with a $-5/3$ slope, and a rather large dissipation range. Further results are presented in the following section, where a comparison of LES and multilevel simulations results with DNS ones is performed.

4.1.2. Large-eddy and multilevel simulations results

In this section, the results from several two-level simulations and from a monolevel LES are compared in detail with those from the DNS. Several quantities have been studied, such as instantaneous mean streamwise velocity profiles and mean velocity fluctuations, kinetic energy spectra, and the temporal evolution of the momentum thickness.

The momentum thickness δ_m is defined by

$$\delta_m(t) = \int_{-L_y/2}^{L_y/2} \left(\frac{1}{4} - \frac{\langle u_1 \rangle_{xz}^2}{\Delta U^2} \right) \mathrm{d}y, \tag{23}$$

where the brackets $\langle \cdot \rangle_{xz}$ denote an averaging over the planes $y = C^{st}$.

All our computations (except the DNS) have been performed on a $64 \times 64 \times 32$ computational grid, referred to as our "fine grid", which is comparable to the 32^3 grid used by Vreman et al. compared to the domain size. For the two-level computations, the "coarse grid" is defined from the fine one by keeping every other grid point in each space direction, leading to the definition of a $32 \times 32 \times 16$ grid. Table 1 summarizes the different computational cases that have been considered, together with the gain factor on the CPU-time required to perform the whole computation in comparison with the CPU-time required to perform the monolevel LES

$$G_{\mathrm{CPU}} = \frac{\text{CPU-time for case "LoMix-LES"}}{\text{CPU-time for considered case}}. \tag{24}$$

These simulations include the DNS, the monolevel LES, and three two-level simulations, two of them being self-adaptive in time. Several tests have been performed to choose the subgrid model at the fine level. The dynamic Smagorinsky model [12] gives the best compromise between the accuracy of the simulation in comparison with DNS and the computational cost of the simulation. In particular, a dynamic mixed model, as proposed in [38] does not improve significantly the accuracy of the simulation, while the computational times are increased in comparison with other classical models. The dynamic Smagorinsky model has thus been retained as subgrid closure at the fine level for all our simulations. In our implementation, numerical instabilities coming from intense negative values of the dynamic coefficient are classically prevented by plane-averaging in the planes of homogeneity (x, z).

As in the DNS, all the simulations that have been performed in this section lead to a fully three-dimensional flow, which becomes fully turbulent around $t = 60$, just before the second pairing.

The time-adaptive behavior of the multilevel simulations with a dynamic value of $N_{\mathrm{it}}^{(2)}$ is illustrated by Fig. 3 showing the temporal evolution of the coarse iteration number $N_{\mathrm{it}}^{(2)}$ performed at each cycle for $\varepsilon_{\max} = 10^{-3}$. Notice that $N_{\mathrm{it}}^{(2)}$ increases during the first part of the simulation which corresponds to the amplification of the most amplified wavelength and to the establishment of the primary large-scale structure, while it decreases just before the second pairing, indicating that a small-scale transition occurs. Finally, $N_{\mathrm{it}}^{(2)}$ reaches a quasi-constant value after the second pairing, when the flow is fully turbulent with a large amount of small scales.

Fig. 4 compares the temporal evolution of the momentum thickness δ_m obtained in each case. It is observed that both the reference monolevel large-eddy simulation and the multilevel simulations slightly delay the sudden growth of the momentum thickness in comparison with the DNS, indicating that the

Table 1
Computational cases and CPU gain factors for the low-Reynolds mixing layer

Case	Grid(s)	$N_x \times N_y \times N_z$	Subgrid model	$N_{\mathrm{it}}^{(n)}$	$\varepsilon_{\max}$	G_{CPU}
LoMix-DNS	1	$256 \times 192 \times 192$	–	1	–	0.009
LoMix-LES	1	$64 \times 64 \times 32$	Dyn.Smag.	1	–	1
LoMix-ML	1	$64 \times 64 \times 32$	Dyn.Smag.	1	–	2.00
	2	$32 \times 32 \times 16$	Multilevel	1		
LoMix-MLdyn1	1	$64 \times 64 \times 32$	Dyn. Smag.	1	10^{-4}	1.93
	2	$32 \times 32 \times 16$	Multilevel	Dyn.		
LoMix-MLdyn2	1	$64 \times 64 \times 32$	Dyn.Smag.	1	10^{-3}	4.13
	2	$32 \times 32 \times 16$	Multilevel	Dyn.		

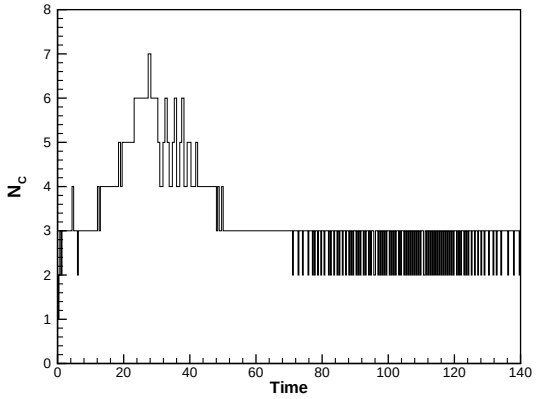

Fig. 3. Coarse iteration number per cycle, case LoMix-MLdyn2 ($\varepsilon_{\max} = 10^{-3}$).

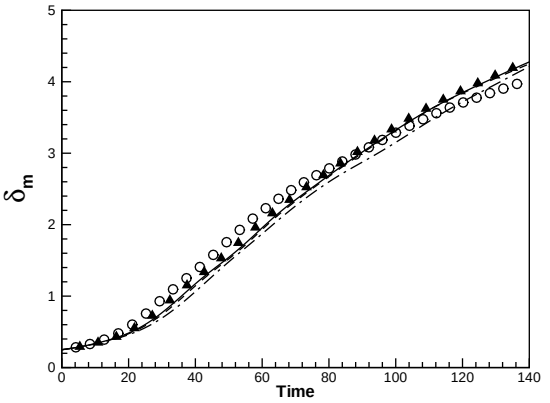

Fig. 4. Momentum thickness δ_m. ○, LoMix-DNS (filtered); ▲, LoMix-LES; - - -, LoMix-ML; —, LoMix-MLdyn1; - · - · -, LoMix-MLdyn2.

primary instabilities of the flow are amplified more slowly. The agreement between the large-eddy and multilevel simulations and the DNS remains however reasonable, and comparable to the results of Vreman et al. [36] presented before the second pairing. Moreover, the agreement between the multilevel simulations and the fine reference LES is good at every time, except perhaps for the case LoMix-MLdyn2, in which a high value of the small-scales error parameter $\varepsilon_{\max}$ slightly delays the development of instabilities and thus the growth of the mixing layer.

Figs. 5 and 6 compare, respectively, the plane-averaged (x–z) streamwise velocity profiles, and the RMS streamwise velocity fluctuations, normalized by $\Delta U = 2U_\infty$, obtained in each case, at the time $t = 100$, as a function of the normalized coordinate $\psi = y/\delta_m$. While the mean profiles are very similar at each filtering level, the fluctuations are slightly larger at the fine level of a multilevel simulation. Indeed, fluctuations at this level reflect the effect of the quasi-static approximation of the highest resolved wavenumbers. For this reason, the fluctuations are computed at the second level of filtering in all our multilevel simulations. A good agreement is observed between the multilevel results, the fine monolevel reference ones, and DNS results at $t = 100$, which is also observed at every time of the simulation. Globally, our results thus demonstrate the potentialities of both classical LES and of the multilevel approach to give some results in good agreement with those from DNS.

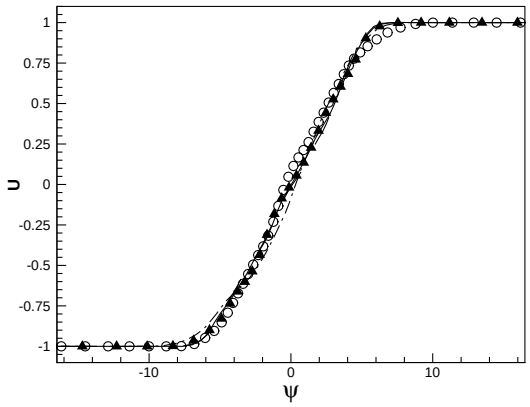

Fig. 5. Streamwise velocity profile at $t = 100$ ∘, LoMix-DNS (filtered); ▲, LoMix-LES; - - -, LoMix-ML; —, LoMix-MLdyn1; - · · · -, LoMix-MLdyn2.

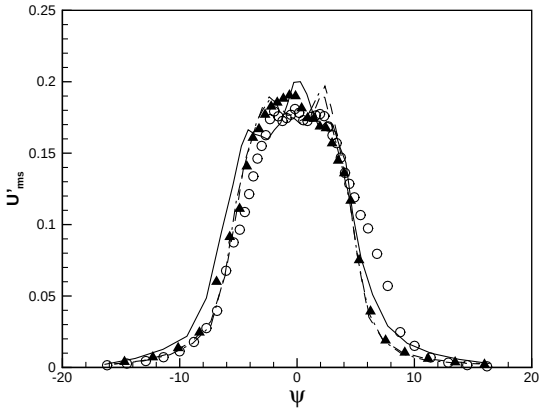

Fig. 6. RMS streamwise velocity fluctuations at $t = 100$. ∘, LoMix-DNS (filtered); ▲, LoMix-LES; - - -, LoMix-ML; —, LoMix-MLdyn1; - · · · -, LoMix-MLdyn2.

Finally, Fig. 7 shows the monodimensional streamwise energy spectrum obtained in each case at the end of the simulation. For all simulations, a general good agreement is obtained, and a short $-5/3$ slope is observed over approximately 15 modes. It is also observed that the two-level simulation performed with the highest value of the small-scales error parameter $\varepsilon_{\max}$ presents some errors on the high wavenumbers, which indicate that the small scales of the flow are kept frozen during a too long time in this simulation, and are affected by the quasi-static approximation.

4.2. Inviscid case

The computational domain considered here is the same as in the low-Reynolds case, but with dimensions $L_x = 1$, $L_y = 40\delta_0$, $L_z = \frac{2}{3}L_x$, where the initial vorticity thickness corresponds again to an eight-eddy calculation: $\delta_0 = 1/7N_{\mathrm{rol}}$ with $N_{\mathrm{rol}} = 8$. The resolution of the fine grid used in our computations is $120 \times 100 \times 60$. The grid is uniform in the streamwise and spanwise directions, while it is refined in the shear layer of the flow $[-L_y/8; L_y/8]$. The coarse grid is defined from the fine one, by keeping every other grid point in each direction.

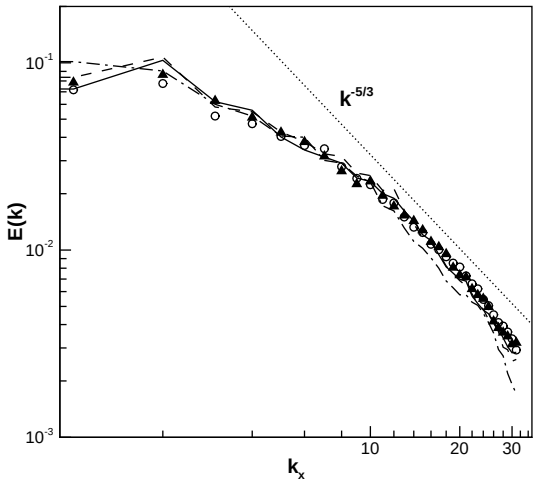

Fig. 7. Streamwise energy spectrum at $t = 140$. ○, LoMix-DNS (filtered); ▲, LoMix-LES; - - -, LoMix-ML; —, LoMix-MLdyn1; - · - · -, LoMix-MLdyn2.

The flow is initiated from the same mean profiles as in the low-Reynolds case. This time, a uniform white noise three-dimensional perturbation, corresponding to the residual turbulence present in experiments, is simply added on these profiles. This perturbation is modulated by the same function $f(y)$ as in the low-Reynolds case, and its amplitude is set to 5×10^{-2}.

The simulation Mach number is still $M = 0.2$, and the Reynolds number is set to a quasi-infinite value of $Re_{\delta_0} = 10^{10}$, so that the dissipation is due to the subgrid terms only, viscous effects becoming negligible.

In this quasi-inviscid case, several flow features are studied in the following. First of all, the purely three-dimensional perturbation used in our computations should lead to the helicoidal pairing configuration discussed by Comte et al. [2], and observed in laboratory experiments. One explanation for this can be the amplification of oblique modes making the primary rollers oscillate and pair off in helix. More details about this phenomenon can be found in [2]. Moreover, for sufficiently long simulation time, the flow should undergo a transition to small scales, and thus the establishment of a Kolmogorov spectrum is expected [2,25]. From many previous works, both in the numerical and experimental contexts, it results that turbulent mixing layers at sufficiently high Reynolds number display a self-similar behavior provided the computational domain is large enough [25,36]. Such a behavior is expected between the second and the third pairings, and corresponds to a temporal range during which the profiles of normalized statistical quantities at different times coincide.

Five different simulations have been performed and compared: one monolevel LES on the fine mesh, and one on the coarse mesh corresponding to the second level of resolution of the multilevel simulations, one standard two-level simulation with $N_{\mathrm{it}}^{(2)}$ fixed to one, and two self-adaptive multilevel simulations with two different values of the parameter $\varepsilon_{\max}$ ($\varepsilon_{\max} = 1 \times 10^{-4}$ and $\varepsilon_{\max} = 1 \times 10^{-3}$). This time, all the simulations use a simple Smagorinsky model as subgrid closure at the finest level of resolution, with a constant value of the coefficient $C_s = 0.18$. Indeed, at this high level of turbulence, experience shows that a dynamic version of the Smagorinsky model is not needed, and that its classical version provides similar results without the overcost in CPU time due to the dynamic procedure. All the computational cases are summarized in Table 2, together with the gain factor on CPU-time in comparison with the fine monolevel LES. Again, the multilevel approach allows to reduce significantly the CPU times, by a factor between 1.8 and 3.5.

Table 2
Computational cases and CPU gain factors for the inviscid mixing layer

Case	Grid(s)	$N_x \times N_y \times N_z$	Subgrid model	$N_{\text{it}}^{(n)}$	$\varepsilon_{\max}$	G_{CPU}
HiMix-LES	1	$120 \times 100 \times 60$	Smag	1	–	1
HiMix-CLES	1	$60 \times 50 \times 30$	Smag	1	–	10.45
HiMix-ML	1	$120 \times 100 \times 60$	Smag	1	–	1.80
	2	$60 \times 50 \times 30$	Multilevel	1		
HiMix-MLdyn1	1	$120 \times 100 \times 60$	Smag	1	10^{-4}	1.97
	2	$60 \times 50 \times 30$	Multilevel	Dyn.		
HiMix-MLdyn2	1	$120 \times 100 \times 60$	Smag	1	10^{-3}	3.50
	2	$60 \times 50 \times 30$	Multilevel	Dyn.		

4.2.1. Flow characteristics

The simulations have been performed from $t = 0$ to 160, with t the time scaled with U_∞ and δ_0. All the simulations exhibit the same physical behavior, except the coarse LES which is less turbulent, and remains quasi-bidimensional. That can be explained by an over-dissipative behavior of the model with the coarse resolution, preventing the development of transverse modes. Moreover, it should be mentioned that in this case, while the simulation is stable, odd–even oscillations can be seen on several variables of the flow, indicating that the resolution is too low for the non-dissipative numerical scheme used here.

On the other hand, the four other simulations exhibit a fully turbulent and three-dimensional behavior, while no wiggles are detected. After the formation of the primary rollers at $t \simeq 30$, a first helicoidal pairing is observed, resulting in a vortex-lattice structure between $t = 60$ and 100. Afterwards, the flow evolves in a small-scale transition.

Fig. 8 compares the temporal evolution of the momentum thickness δ_{m} obtained in each case. First, it is observed that the coarse monolevel simulation has a very different behavior. In particular, the sudden growth of the mixing layer starts only around $t = 110$, while it starts around $t = 50$ for all the other simulations. Fig. 9 shows the temporal decrease of kinetic energy in the whole computational domain. Again, it is striking that the multilevel simulations have the same behavior as the fine monolevel reference simulation, while the coarse grid simulation is very different. In this last case, the decrease of kinetic energy is stronger in the first part of the simulation, while it is very slow after $t = 80$. This is due to the fact that the purely dissipative Smagorinsky closure used on the coarse grid is too dissipative during the first part of the simulation, leading to a quasi two-dimensional flow in which no transition to small scales occurs. On

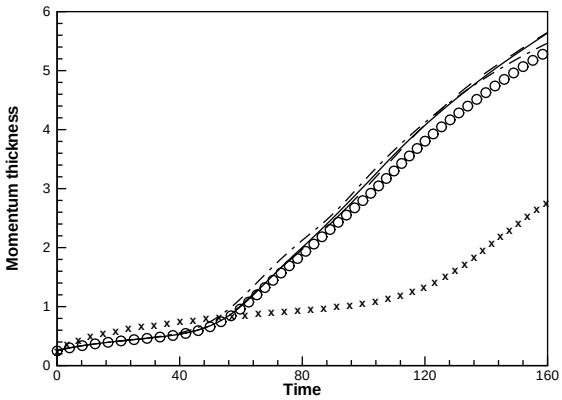

Fig. 8. Momentum thickness δ_{m}. ×, HiMix-CLES; ○, HiMix-LES; - - -, HiMix-ML; —, HiMix-MLdyn1; - · - · -, HiMix-MLdyn2.

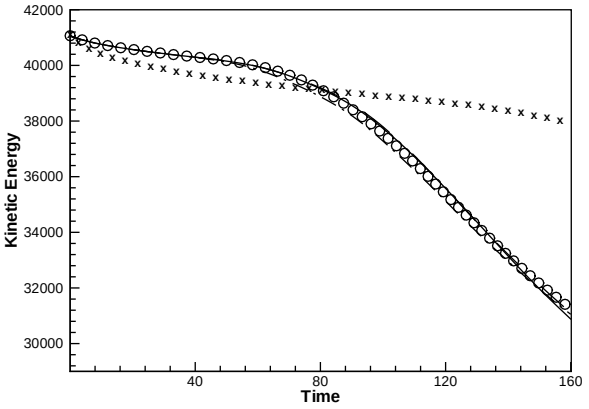

Fig. 9. Total kinetic energy. ×, HiMix-CLES; ○, HiMix-LES; - - -, HiMix-ML; —, HiMix-MLdyn1; - · - · -, HiMix-MLdyn2.

the other hand, the fine monolevel LES and the multilevel simulations exhibit a fully three-dimensional behavior, with a small-scale transition resulting in a higher loss of energy by small-scale cascade.

The small-scale mixing transition is confirmed by three-dimensional visualizations of the flow, and also by Fig. 12 showing at $t = 160$ the presence of a $k^{-(5/3)}$ Kolmogorov spectrum. One can appreciate the fact that for the multilevel simulations, no discontinuity appears around the coarse level cut-off wavenumber k_2. In these simulations, even the highest wavenumbers $k_2 < k < k_1$ appear well resolved, despite the quasi-static approximation, except as in the low-Reynolds case for the self-adaptive simulation performed with $\varepsilon_{\max} = 10^{-3}$. Indeed, some small errors are visible on the highest resolved wavenumbers in that case, indicating that they are affected by the quasi-static approximation, which is performed during a too long time. However, the two other multilevel simulations follow very well the $-5/3$ slope at high wavenumbers, even better than the fine monolevel simulation.

4.2.2. Statistical quantities

Figs. 10 and 11 compare, respectively, the plane-averaged (x–z) mean streamwise velocity profiles, and the RMS streamwise velocity fluctuations, normalized by $\Delta U = 2U_\infty$, obtained in each case, at the time $t = 100$. A general good agreement is obtained between the multilevel results and the fine monolevel reference ones, while the coarse simulation leads to very different results. Some discrepancies between the multilevel simulations and the reference fine one are observed as time advances, but remain small. Moreover, one have to keep in mind that the flow becomes more turbulent as time advances, and thus very dependent to the subgrid closure used.

4.2.3. Self-similarity

At a sufficiently high Reynolds number, numerical simulation of an eight-eddy mixing layer should display a self-similar state between the second and the third pairings, i.e., when the simulation displays the most physical behavior (the unphysical initial perturbations have disappeared, and the simulation does not saturate because another pairing is allowed in the computational box).

This property is analyzed by plotting statistical quantities (here the RMS streamwise velocity fluctuations) in normalized units at different times. During the self-similar phase, if any, the curves should then coincide. From our computations, it results that the coarse simulation does not reach a self-similar state, while both the fine monolevel one, and all the multilevel simulations do, and display a self-similar behavior between the second and the third pairings. Fig. 13 shows the normalized RMS streamwise velocity fluctuations at different times for these simulations, as a function of the normalized coordinate $\psi = y/\delta_m$.

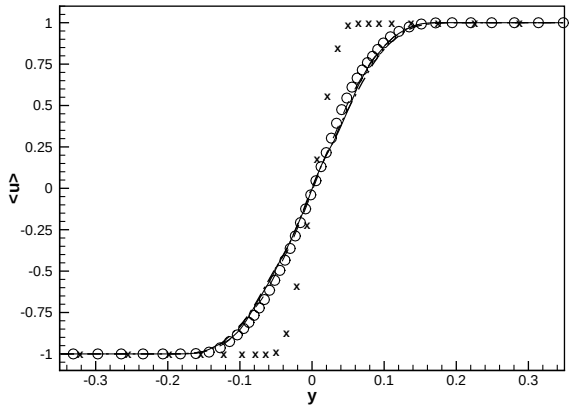

Fig. 10. Streamwise velocity profile at $t = 100$. ×, HiMix-CLES; ○, HiMix-LES; - - -, HiMix-ML; —, HiMix-MLdyn1; - · - · -, HiMix-MLdyn2.

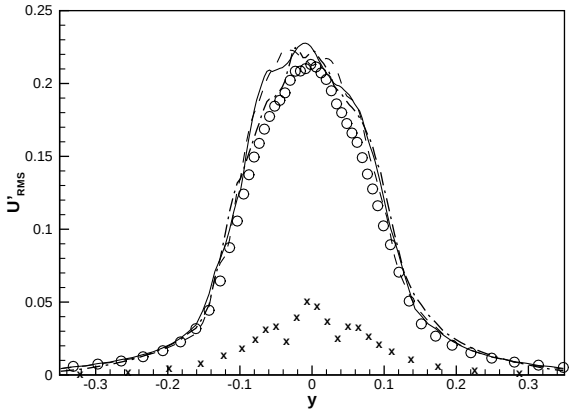

Fig. 11. RMS streamwise velocity fluctuations at $t = 100$. ×, HiMix-CLES; ○, HiMix-LES; - - -, HiMix-ML; —, HiMix-MLdyn1; - · - · -, HiMix-MLdyn2.

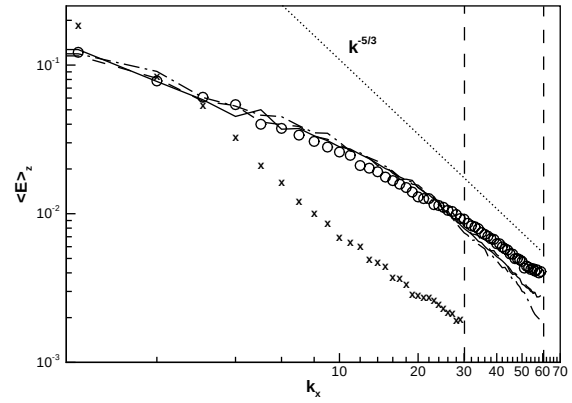

Fig. 12. Streamwise energy spectrum at $t = 160$. ×, HiMix-CLES; ○, HiMix-LES; - - -, HiMix-ML; —, HiMix-MLdyn1; - · - · -, HiMix-MLdyn2.

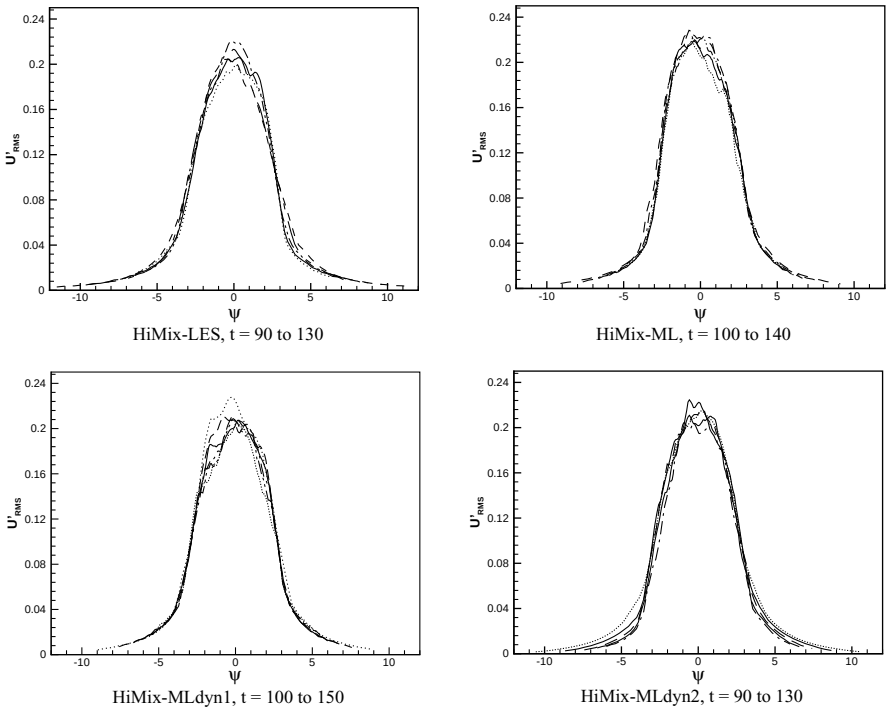

Fig. 13. RMS streamwise velocity fluctuations during the self-similar phase.

4.2.4. Intergrid energy transfers analysis

In this section, the action of the subgrid closure used on the coarse grid is analyzed more in detail. Indeed, this term controls the processes of energy transfers between the two grid levels.

Usually, the subgrid energy transfers at each level of resolution are analyzed through the dissipation ε defined as

$$\varepsilon = -\tau^{(n)} : \nabla\left(\frac{\overline{\rho U}^{(n)}}{\overline{\rho}^{(n)}}\right) = -\tau^{(n)} : \overline{S}^{(n)}, \tag{25}$$

where $\tau^{(n)}$ is the classical subgrid stress tensor of the level n

$$\tau^{(n)} = \overline{\rho U \otimes U}^{(n)} - \overline{\rho U}^{(n)} \otimes \overline{\rho U}^{(n)}/\overline{\rho}^{(n)}. \tag{26}$$

In the present case, no explicit computation of the subgrid stress-tensor is performed on the coarse level. Instead, the subgrid term $\mathscr{T}^{(2)}$ is directly computed, and is equivalent to the SGS forces

$$\mathscr{T}^{(2)}_{i+1} \equiv N_i = (\nabla \cdot (\tau^{(2)}))_i \tag{27}$$

for $i = 1$–3. Thus, in the present case, the only computable quantity are the SGS forces, and the associated energy transfer term T

$$T = \frac{\overline{\rho U}^{(2)}}{\overline{\rho}^{(2)}} \cdot N = \frac{\overline{\rho U}^{(2)}}{\overline{\rho}^{(2)}} \cdot \nabla \cdot (\tau^{(2)}). \tag{28}$$

This term appears in the resolved kinetic energy balance equation when commutation of the filtering operation with space derivatives is assumed, and describes the exchange of energy between resolved and subgrid scales.

In fact, this term is the sum of two terms:

$$T = \varepsilon + \nabla \cdot (\tau^{(2)} \cdot (\overline{\rho U}^{(2)}/\overline{\rho}^{(2)})).$$

That is to say that the global subgrid energy transfer defined by (28) takes into account the subgrid dissipation, but also a spatial transport of energy.

This term appears directly in the rhs of the resolved and subgrid kinetic energy equations, with negative and positive signs, respectively. Thus, positive values of T mean that energy is lost by the resolved field. Since only plane-averaged profiles are generally plotted, it is also interesting to evaluate the quantities $T^+ = \max(T, 0)$ and $T^- = \min(T, 0)$, to give a more local information about the energy transfers. However, it remains not possible to distinguish precisely spatial transport of energy from subgrid dissipation.

Fig. 14 presents the plane-averaged profiles of T, T^+, and T^- for the multilevel simulation with $\varepsilon_{\max} = 10^{-4}$, at the four different times $t = 20,\ 60,\ 100,$ and 140. It appears that during all the simulation, $\langle T \rangle$ remains positive, showing that energy is continuously lost in mean by the resolved field. In the fully turbulent regime, the amplitude of $\langle T^+ \rangle$ and $\langle T^- \rangle$ is roughly five times the one of $\langle T \rangle$, thus indicating that there is a large fluctuation (including backscatter) of the energy transfer.

5. Application 2: plane channel flow

The aim of this part is to assess the multilevel closure and cycling strategy in the case of wall-bounded flows. The considered test case is the well-referenced plane channel flow configuration, which consists in a

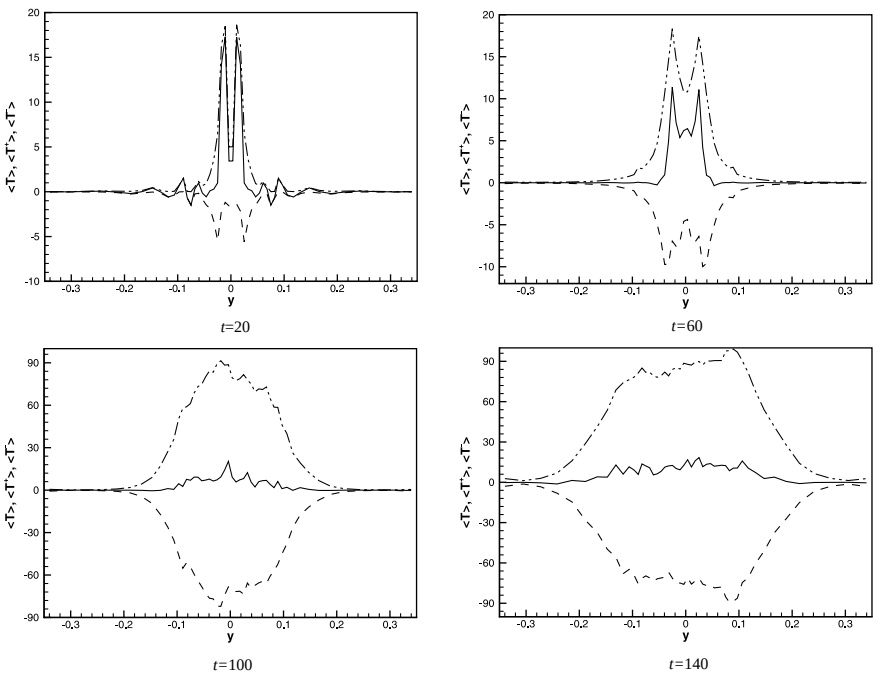

Fig. 14. Intergrid energy transfer term in the case HiMix-MLdyn1 ($\varepsilon_{\max} = 10^{-4}$). Intergrid energy transfer term in the case HiMix-MLdyn1 ($\varepsilon_{\max} = 10^{-4}$). —, $\langle T \rangle$; - · - · -, $\langle T^+ \rangle$; - - -, $\langle T^- \rangle$.

turbulent flow between two parallel infinite isothermal (cold) walls. It is again a typical example of a multiscale problem, since large structures dominate in the core region of the channel, while the near-wall dynamic of the flow is dominated by small coherent structures in the viscous layer, the streaks, which require a deterministic resolution.

The flow is initiated by a parabolic laminar Poiseuille mean flow, on which a random white-noise is added to initiate transition to turbulence. To compensate the loss of energy due to viscous forces, the flow is driven by a forcing term, which is adjusted dynamically in time, following the numerical algorithm proposed by Lenormand et al. [20,21]. This algorithm ensures a constant mass flux through the channel. More details about the computational case can be found in [20] or in [34].

The Reynolds number value based on the mean bulk velocity and density, the channel half-width and the viscosity at the wall is 10,925, corresponding to a skin-friction Reynolds number of about 590. For this case, reference results from incompressible Direct Numerical Simulations are available in the paper of Moser et al. [23]. They are used as reference in the present study, together with the results from fine monolevel large-eddy simulations performed with the dynamic Smagorinsky model. As in the mixing-layer configuration, the model is stabilized by plane-averages in the planes of homogeneity. The Mach number of the simulations has been set to 0.5, which is small enough to compare our results with incompressible ones (a maximum variation of 4% is observed on density).

Multilevel simulations have then been performed and compared to the reference results. These simulations are self-adaptive two-level simulations with the value of the parameter $\varepsilon_{\max}$ set to 10^{-4}, and two three-level simulations: one with a constant value of one time step satisfying the CFL condition performed at each level (e.g., $N_{\text{it}}^{(n)} = 1$ for $n = 1$–3), and one with both a dynamic value of the number of levels and $N_{\text{it}}^{(n)}$. In this last case, the small-scales error parameter has been set to an intermediate value between 10^{-4} which does not allow time integration on a third level, and 10^{-3} which is to high, as it has been seen in the mixing layer section. The number of levels to be considered is always three in practice in this case.

All the computational cases considered in this section are summarized in Tables 3 and 4, which also show the computed skin-friction Reynolds number, and the computational CPU gain factor obtained in the multilevel case in comparison with the fine monolevel LES. The computational grids used in each case are uniform in the streamwise (x) and spanwise (y) directions, while grid stretching is used in the wall-normal direction (z) by mean of an hyperbolic tangent-law progression, which ensures that the first grid point is at $z^+ = 1$ away from the wall. The domain dimensions in the respective x, y, and z directions are $2\pi \times \pi \times 2$.

First, it is interesting to note again the significant cost reduction provided by the multilevel approach in terms of CPU-time requirement in comparison with the monolevel LES. Indeed, the CPU gain factor is larger than two for the two-level simulations, and nearly reaches five for the three-level one. In all cases, the

Table 3
Computational cases for the plane channel flow simulations

Case	Re	Grid(s)	$N_x \times N_y \times N_z$; $(\Delta x^+ \times \Delta y^+ \times \Delta z^+_{\min})$	Subgrid model
HiChan-DNS	10,925	1	$384 \times 257 \times 384$; $(9.7 \times 4.8 \times 0.044)$	–
HiChan-LES	10,925	1	$52 \times 120 \times 128$; $(71 \times 15.4 \times 1)$	Dyn.Smag.
HiChan-MLdyn	10,925	1	$52 \times 120 \times 128$; $(71 \times 15.4 \times 1)$	Dyn.Smag.
		2	$26 \times 60 \times 64$; $(142 \times 30.8 \times 2)$	Multilevel
HiChan-ML3G	10,925	1	$52 \times 120 \times 128$; $(71 \times 15.4 \times 1)$	Dyn.Smag.
		2	$26 \times 60 \times 64$; $(142 \times 30.8 \times 2)$	Multilevel
		3	$13 \times 30 \times 32$; $(284 \times 61.6 \times 4.4)$	Multilevel
HiChan-ML3Gdyn	10,925	1	$52 \times 120 \times 128$; $(71 \times 15.4 \times 1)$	Dyn.Smag.
		2	$26 \times 60 \times 64$; $(142 \times 30.8 \times 2)$	Multilevel
		3	$13 \times 30 \times 32$; $(284 \times 61.6 \times 4.4)$	Multilevel

DNS cases are taken from [23].

Table 4
Computational parameters, integrated friction Reynolds numbers, and CPU gain factors for the plane channel flow simulations

Case	$N_{it}^{(1)}/N_{it}^{(2)}/N_{it}^{(3)}$	ε_{max}	Re_τ (% error)	G_{CPU}
HiChan-DNS	1/–/–	–	587 (−0.5%)	–
HiChan-LES	1/–/–	–	581 (−1.5%)	1
HiChan-MLdyn	1/Dyn/–	10^{-4}	596 (+1.0%)	2.20
HiChan-ML3G	1/1/1	–	579 (−1.9%)	4.72
HiChan-ML3Gdyn	1/Dyn/Dyn	5×10^{-4}	582 (−1.3%)	5.00

agreement of the computed skin-friction Reynolds number value with the targeted value is very good, with a maximum relative error of only 1.9% for one of the three-level computations.

Fig. 15 presents the mean (plane- and time-averaged) streamwise velocity profiles obtained, in wall units, together with the theoretical wall laws $u^+ = z^+$ and $u^+ = 1/K \log(z^+) + 5.5$, where K is the Von Karman constant ($K \simeq 0.4$). A difference is observed in the logarithmic zone between the LES results and the DNS and wall law. Indeed, the slope is not the same, and reflects an over-estimation of the Von Karman constant present in the theoretical laws. This is a common observation for all the channel flow LES performed with a second-order spatial scheme combined with a relatively coarse grid resolution. Indeed, one can refer for instance to the works of Kravchenko and Moin [19] who studied in detail the influence of the accuracy of the spatial scheme on the results in the plane channel flow configuration. Similar discrepancies also occur in LES based on spectral methods with sufficiently coarse resolution. This can be explained by the lack of resolution of near-wall processes which cannot be accounted for by subgrid models. However, the results obtained with the multilevel simulations appear to be in good agreement with the fine monolevel LES, and even in a slightly better agreement with DNS for the two-level self-adaptive simulation.

Fig. 16 presents the mean resolved turbulent kinetic energy profiles. All our simulations over-estimate the peak value in comparison with DNS, while its position is well predicted, at $z^+ \simeq 18$ away from the wall. This is again due to the second order spatial scheme and the rather coarse grid resolution used in our simulations. The two-level self-adaptive simulation leads to results in very good agreement with the fine monolevel ones. For the three-level computations, it is observed that the run HiChan-ML3G performed with a fixed value of $N_{it}^{(n)}$ overestimates the peak value of the resolved turbulent kinetic energy of approximately 16% in comparison with the fine monolevel LES, while the simulation HiChan-ML3Gdyn, performed with the self-adaptive cycling strategy overestimates the peak value of only 4.5%. Indeed, in this

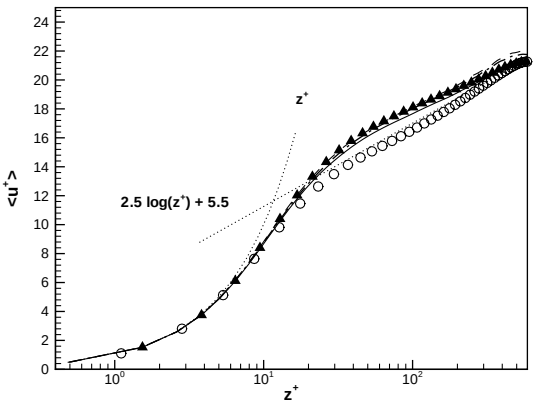

Fig. 15. Mean streamwise velocity: $Re_\tau = 590$. ○, HiChan-DNS; ▲, HiChan-LES; —, HiChan-MLdyn; - - -, HiChan-ML3G; - · · · -, HiChan-ML3Gdyn.

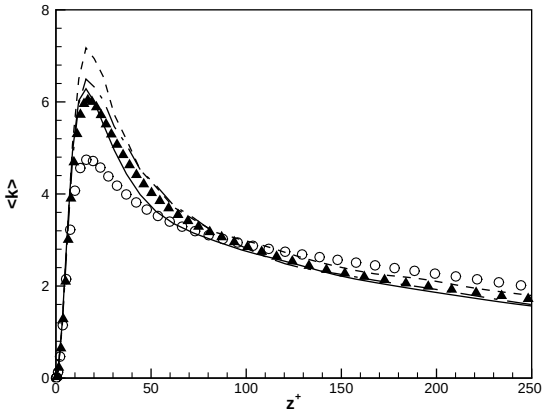

Fig. 16. Mean resolved turbulent kinetic energy: $Re_\tau = 590$. ○, HiChan-DNS; ▲, HiChan-LES; —, HiChan-MLdyn; - - -, HiChan-ML3G; - · - · -, HiChan-ML3Gdyn.

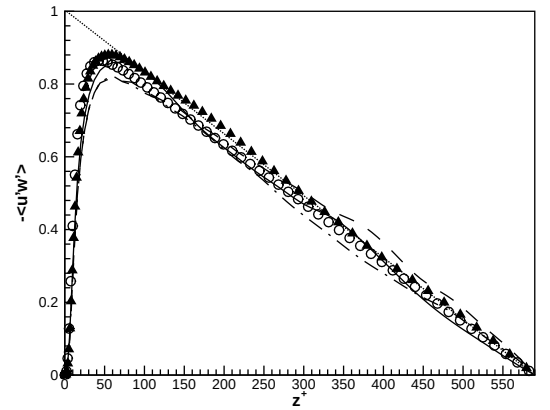

Fig. 17. Mean resolved turbulent kinetic energy: $Re_\tau = 590$. ○, HiChan-DNS; ▲, HiChan-LES; —, HiChan-MLdyn; - - -, HiChan-ML3G; - · - · -, HiChan-ML3Gdyn.

last simulation, the error commited on the high wavenumbers of the flow is well controlled by the self-adaptive strategy. Moreover, the CPU gain factor obtained in this case is slightly higher than in the non-adaptive simulation. In the self-adaptive simulation, more time is spent on the second grid level, and less time on the third grid level (the CFL is reduced on this grid) than in the non-adaptive one. This results in slightly longer V-cycles, and in a reduction of the error commited during time integration on the third grid level.

Resolved and total Reynolds shear stress are plotted on Figs. 17 and 18, respectively, and show a general good agreement of the multilevel simulations with monolevel LES and DNS reference results. Fig. 19 displays the resolved vorticity fluctuations obtained in each case. While the overall agreement between the multilevel and monolevel simulations is correct, the level of vorticity fluctuation appears to be lower in the case of the three-level simulations, thus indicating a slightly lower level of turbulence.

It should however be mentioned that the three-level simulations are still able to accurately describe the near-wall dynamic of the flow, while CPU-times are reduced by a factor of up to five. In particular, instantaneous three-dimensional visualizations of the flow highlight the presence of the near-wall streaks.

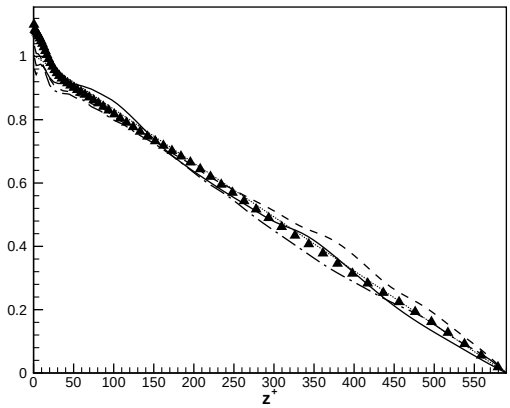

Fig. 18. Mean resolved turbulent kinetic energy: $Re_\tau = 590$. ▲, HiChan-LES; —, HiChan-MLdyn; - - -, HiChan-ML3G; - · - · -, HiChan-ML3Gdyn.

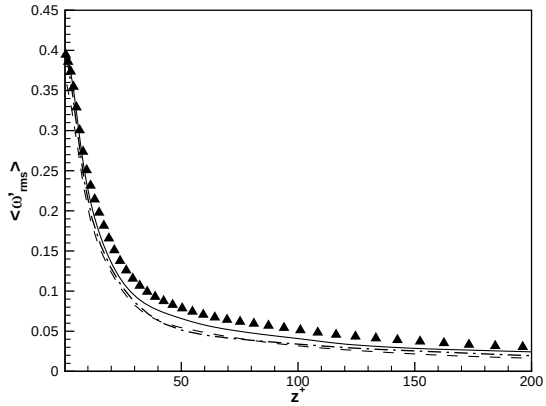

Fig. 19. Mean resolved turbulent kinetic energy: $Re_\tau = 590$. ▲, HiChan-LES; —, HiChan-MLdyn; - - -, HiChan-ML3G; - · - · -, HiChan-ML3Gdyn.

These fine structures are well-captured by the simulation, while they are not resolved at all on the third grid level which is too coarse.

Finally, Fig. 20 shows the mean subgrid energy transfer term appearing in the filtered energy equation at level two, for the HiChan-MLdyn simulation. It is observed that this term describes very well the dynamic of the flow. Indeed, in the near-wall region, this term is positive, while it becomes negative away from the wall. This indicates that the large scales in the near-wall region $0 < z^+ < 20$ are losing energy, which is either dissipated by interactions with subgrid scales, either transferred to the core region of the channel. Indeed, the near-wall zone corresponds to the production zone of the channel, where energy is produced and transferred to the center of the channel and to the walls.

6. Conclusions

A multilevel methodology to perform LES of compressible flows at lower cost has been presented and assessed in a time-developing mixing layer configuration and a plane channel flow.

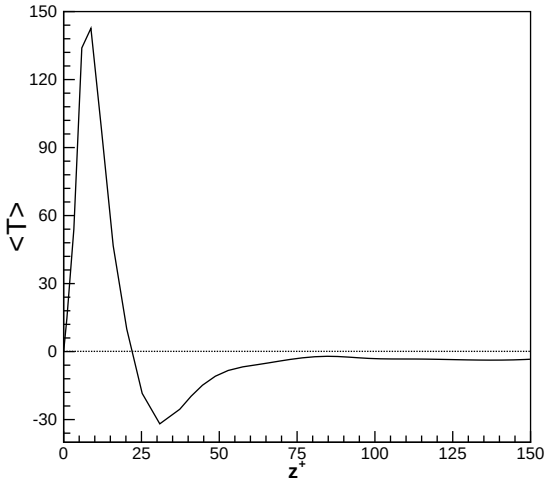

Fig. 20. Mean subgrid energy transfer term at level two in the HiChan-MLdyn case.

This method is based on a quasi-static approximation of the small scales, and a dynamic time self-adaptive algorithm based on an a priori error estimate has been proposed to ensure the validity of this approximation in fully unsteady cases. This algorithm uses a V-cycling strategy between nested computational grids in physical space, and estimates dynamically both the number of levels and the time that can be spent on each level.

A new closure based on a multilevel generalization of Germano's identity has been presented in Section 2.3 to close the filtered equations on the coarse levels. This closure uses more information than standard LES closures, since the high-wavenumber deterministic information from the finer levels is directly taken into account. The closure at the finest level of filtering is done by the use of a classical LES model. Indeed, the method applies to any fundamental LES closure at the fine level.

Globally, it results that the multilevel closure proposed is very efficient, and allows to get results in good agreement with fine monolevel LES, while the CPU-time requirement of the simulation are significantly reduced by a factor between two and five. It has also been shown that the time self-adaptive procedure allows in some case to improve the results in comparison with non-adaptive multilevel computations, as in the three-level channel flow simulation, while an additional CPU-time reduction can be expected, reaching a factor of five for three-level computations. However, the use of more than two filtering levels still implies that the coarsest grid has a reasonable number of meshpoint to perform a simulation, i.e., a "reasonable" coarse LES. It is thus limited to the simulation of flows in which fine computational grids are used at the finest level, as the high Reynolds number channel flow in the present paper. Elsewhere, the algorithm applied with more than two levels would at minimum produce some results that can be used to initiate quickly more accurate simulations. Two-level simulations however appear as a very good compromise with a CPU gain factor of two, and results as accurate as those from fine monolevel LES.

Finally, while the present method has been presented as an acceleration technique, it should be mentioned that it is a general multilevel approach which can be classified in other ways. Indeed, it can also be seen as a deconvolution-like approach if the computation is performed at the coarsest level while the finer ones are only used to compute the subgrid terms, or as a more general combined approach if the computation grid corresponds to an intermediary level. In these last two cases, the fundamental aspect of the method should then be a more general closure than classical eddy-viscosity ones.

Acknowledgements

The authors thank Dr. P. Comte for useful discussions about the mixing layer case.

References

[1] D. Carati, A.A. Wray, Time filtering in large eddy simulation, in: Proceedings of the Summer Program 2000, Center for Turbulence Research, 2000, pp. 263–270.
[2] P. Comte, M. Lesieur, E. Lamballais, Large- and small-scale stirring of vorticity and a passive scalar in a 3-D temporal mixing layer, Phys. Fluids A 4 (12) (1992) 2761–2778.
[3] Y.M. Dakhoul, K.W. Bedford, Improved averaging method for turbulent flow simulation. Part 1: theoretical development and application to burger's transport equation, Int. J. Numer. Methods Fluids 6 (1986) 49–64.
[4] Y.M. Dakhoul, K.W. Bedford, Improved averaging method for turbulent flow simulation. Part 2: calculations and verification, Int. J. Numer. Methods Fluids 6 (1986) 65–82.
[5] A. Debussche, T. Dubois, R. Temam, The nonlinear galerkin method: a multi-scale method applied to the simulation of homogeneous turbulent flows, ICASE Report No. 93-93, December 1993.
[6] J.A. Domaradzki, W. Liu, C. Härtel, L. Kleiser, Energy transfer in numerically simulated wall-bounded turbulent flows, Phys. Fluids 6 (4) (1994) 1583–1599.
[7] J.A. Domaradzki, K.C. Loh, The subgrid-scale estimation model in the physical space representation, Phys. Fluids 11 (8) (1999) 2330–2342.
[8] J.A. Domaradzki, E.M. Saiki, A subgrid-scale model based on the estimation of unresolved scales of turbulence, Phys. Fluids 9 (7) (1997) 2148–2164.
[9] J.A. Domaradzki, P.P. Yee, The subgrid-scale estimation model for high Reynolds number turbulence, Phys. Fluids 12 (1) (2000) 193–196.
[10] T. Dubois, F. Jauberteau, R. Temam, Incremental unknowns, multilevel methods and the numerical simulation of turbulence, Comput. Methods Appl. Mech. Engrg. 159 (1998) 123–189.
[11] M. Germano, A proposal for a redefinition of the turbulent stresses in the filtered Navier–Stokes equations, Phys. Fluids 29 (7) (1986) 2323–2324.
[12] M. Germano, U. Piomelli, P. Moin, W.H. Cabot, A dynamic subgrid-scale eddy viscosity model, Phys. Fluids A 3 (1991) 1760–1765.
[13] A. Harten, Multiresolution representation of data: a general framework, SIAM J. Numer. Anal. 33 (3) (1996) 1205–1256.
[14] L.-H. Huang, C-H. Ho, Small-scale transition in a plane mixing layer, J. Fluid Mech. 210 (1990) 475–500.
[15] T.J.R. Hugues, L. Mazzei, A.A. Oberai, The multiscale formulation of large eddy simulation: decay of homogeneous isotropic turbulence, Phys. Fluids 12 (2) (2001) 505–512.
[16] T.J.R. Hugues, A.A. Oberai, L. Mazzei, Large eddy simulation of turbulent channel flows by the variational multiscale method, Phys. Fluids 12 (6) (2001) 1784–1799.
[17] M.R. Kerr, J.A. Domaradzki, G. Barbier, Small-scale properties of nonlinear interactions and subgrid-scale energy transfer in isotropic turbulence, Phys. Fluids 8 (1996) 197.
[18] R.H. Kraichnan, Inertial-range transfer in two- and three-dimensional turbulence, J. Fluid Mech. 47 (3) (1971) 525–535.
[19] A.G. Kravchenko, P. Moin, On the effect of numerical errors in large eddy simulation of turbulent flows, J. Comput. Phys. 131 (1997) 310–322.
[20] E. Lenormand, P. Sagaut, L. Ta Phuoc, Large-eddy simulation of compressible channel flow at moderate Reynolds number, Int. J. Numer. Methods Fluids 32 (2000) 369–406.
[21] E. Lenormand, P. Sagaut, L. Ta Phuoc, P. Comte, Subgrid-scale models for large-eddy simulation of compressible wall bounded flows, AIAA J. 38 (8) (2000) 1340–1350.
[22] J. Maurer, M. Fey, A scale-residual model for large-eddy simulation, in: Direct and Large-Eddy Simulation III, Kluwer Academic Publishers, Dordrecht, MA, 1999, pp. 237–248.
[23] R. Moser, J. Kim, N.N. Mansour, Direct numerical simulation of turbulent channel flow up to $Re_\tau = 590$, Phys. Fluids 11 (4) (1999) 943–945.
[24] R.D. Moser, M.M. Rogers, Mixing transition and the cascade to small scales in a plane mixing layer, Phys. Fluids A 3 (5) (1991) 1128–1134.
[25] R.D. Moser, M.M. Rogers, Direct simulation of a self-similar turbulent mixing layer, Phys. Fluids A 6 (1994) 903–924.
[26] C.D. Pruett, Eulerian time-domain filtering for spatial large-eddy simulation, AIAA J. 38 (9) (2000) 1634–1642.
[27] S.A. Ragab, J.L. Wu, Linear instabilities in two-dimensional compressible mixing layers, Phys. Fluids A 1 (1989) 957–966.
[28] P. Sagaut, Large-eddy Simulation for Incompressible Flows. Scientific Computation, second ed., Springer, Berlin, 2002.

[29] P. Sagaut, R. Grohens, Discrete filters for large-eddy simulation, Int. J. Numer. Methods Fluids 31 (1999) 1195–1220.
[30] P. Sagaut, E. Labourasse, P. Quéméré, M. Terracol, Multiscale approaches for unsteady simulation of turbulent flows, Int. J. Nonlinear Sci. Numer. Sim. 1 (4) (2000) 285–298.
[31] K.B. Shah, J.H. Ferziger, A new non-eddy viscosity subgrid-scale model and its application to channel flow, in: Annual Research Briefs, Center for Turbulence Research, 1995, pp. 73–90.
[32] S. Stolz, N.A. Adams, L. Kleiser, The approximate deconvolution model applied to LES of turbulent channel flow, in: Direct and Large-Eddy Simulation III, Kluwer Academic Publishers, Dorderecht, MA, 1999, pp. 163–174.
[33] S. Stolz, N.A. Adams, An approximate deconvolution procedure for large-eddy simulation, Phys. Fluids 11 (7) (1999) 1699–1701.
[34] M. Terracol, P. Sagaut, C. Basdevant, A multilevel algorithm for large eddy simulation of turbulent compressible flows, J. Comput. Phys. 167 (2) (2001) 439–474.
[35] P.R. Voke, Multiple mesh simulation of turbulent flow, Report QMW EP-1082, University of London, 1990.
[36] B. Vreman, B. Geurts, H. Kuerten, Large-eddy simulation of the turbulent mixing layer, J. Fluid Mech. 339 (1997) 357–390.
[37] C. Weber, F. Ducros, A. Corjon, Large-eddy simulation of complex turbulent flows, AIAA Paper 98-2651, 1998.
[38] Y. Zang, R.L. Street, J.R. Koseff, A dynamic mixed subgrid-scale model and its applications to turbulent recirculating flows, Phys. Fluids A 5 (12) (1993) 3186–3196.